

# PREDICTION OF HELICOPTER MANEUVER LOADS USING A COUPLED CFD/CSD ANALYSIS

**Jayanarayanan Sitaraman, Beatrice Roget**  
**National Institute of Aerospace**  
**Hampton, Virginia**

**Keywords:** *Helicopter, FSI, maneuver*

## Abstract

*A fluid-structure analysis framework which couples Computational Fluid Dynamics (CFD) and Computational Structural Dynamics (CSD) is constructed to study the aero-mechanics of a helicopter rotor system under maneuvering flight conditions. The CFD approach consists of the solution of Unsteady Reynolds Average Navier Stokes (URANS) equations for the near-field of the rotor coupled with the dynamics of trailed vortex wake that are computed using a free vortex method. The CSD approach uses a multi-body Finite Element method to model the rotor hub and blades. The analysis framework is used to study the Utility Tactical Transport Aerial System (UTTAS) pull-up maneuver of the UH-60A helicopter. Results shown illustrate the correlation of predicted performance, aerodynamic and structural dynamic loading with measured flight test data. The normal load factor and the peak-to-peak structural and aerodynamic loading show good correlation with flight test data, indicating that the analysis framework is suitable for preliminary design purposes. Important phenomena such as advancing blade transonic effects and retreating blade flow separation are predicted satisfactorily. However, deficiencies are noted in the accurate resolution of stall incidence, reattachment and shock induced separation.*

## 1 Introduction

Helicopter rotor systems operate in highly unsteady flow conditions which are characterized by transonic flows, dynamic stall events and returning wake interactions. In addition, there is a large extent of aeroelastic coupling owing to the slender construction of the blades. All these factors contribute to make the prediction of aerodynamic and structural dynamic loading on helicopter rotors a very challenging problem even in steady forward flight. Maneuvering rotorcraft further augments this challenge, because of additional aerodynamic and structural effects due to the hub motion and associated wake transients.

The simulation tools for rotorcraft analysis (termed Comprehensive Aeroelastic Analyses) have historically been using lifting line based aerodynamic models (with suitable enhancements that use table lookup, unsteady flow and stall models). However, such models are known to have inaccurate prediction capabilities [1]. There are two main reasons for the inaccuracies in the lifting line models. The first is the inability to resolve unsteady transonic effects and second is the inability to accurately resolve the returning wake effects [2]. The advent of the CFD (Computational Fluid Dynamics)/CSD (Computational Structural Dynamics) coupled approach replaces the lifting line aerodynamic model with a higher fidelity Computational Fluid Dynamic model that solves the Reynolds-Averaged Navier-Stokes (RANS) equations. This methodology has led to con-

siderable improvements in the airload prediction as demonstrated by various research efforts [2, 3, 4, 5, 6]. The primary reason for the improvement can be attributed to accurate prediction of aerodynamic loading, especially the pitching moments caused by unsteady transonic flows and improved representation of returning wake effects [3].

An important aspect of CFD based aerodynamic load prediction methodologies is the resolution of the wake structures. There are two well established methodologies that are in use at the moment for wake predictions. They are a) wake coupling [7] and b) wake capturing [3, 4, 8]. In the wake coupling methodology, the geometry of the vortex wake, circulation strength and core growth rate are computed externally by solving the vorticity transport equation. The wake positions so obtained are embedded into the RANS-based CFD analysis using the field velocity approach [9]. The wake capturing methodology, in contrast, models the entire rotor system and attempts to capture the wake structure as part of the solution. The advantages of the wake coupling methodology are computational efficiency and ease of modeling. However, it suffers from the empiricism that is used to model the physical diffusion of vorticity. The wake capturing methodology has the advantage of being a first-principle based modeling technique without any empiricism. However, it does suffer from high computational cost and numerical diffusion in predicting the wake structure. An evaluation of the wake coupling and wake capturing methodologies for prediction of steady flight conditions can be found in Ref [10].

The main focus of most recent research efforts was on predicting rotor airloads in steady flight conditions. The periodic nature of the flow field and structural response facilitates the use of the so-called 'loose coupling' approach for interfacing the CFD and CSD analysis modules. In the loose coupling approach, the analysis modules exchange relevant data only every rotor revolution. The inherent decoupling within a revolution provided a fast and robust way for establishing aircraft trim and a fully periodic structural

response. In contrast, simulating an unsteady helicopter maneuver necessitates the exchange of forces and motions at every time step between the fluid and structure methodologies.

Recently, Bhagwat et al. [11, 12] performed the seminal studies on computing airloads and blade loads for the UH-60A pull-up maneuver using a CFD/CSD analysis that coupled OVERFLOW-2 (wake capturing CFD) and RCAS (CSD+ comprehensive analysis) [4]. Remarkable improvements were demonstrated in the prediction of aerodynamic and structural dynamic loads compared to conventional comprehensive analysis. This study triggered a lot of interest in the application of CFD/CSD coupling analysis to simulate helicopter maneuvering flight. Abhishek et al. [13] coupled a simplified aerodynamic model with multi-body CSD analysis. The results obtained were satisfactory for peak-to-peak loading especially for the pushrod loads, however the details of loading waveforms showed unexplained phase differences. Silbaugh et al. [14] used a wake capturing CFD approach coupled with a simplified structural dynamic model. This study concentrated on isolating the differences between the time accurate and serial-staggered coupling approaches and performed simulations only for the first 15 revolutions of the maneuver.

The objective of the present work is to further validate and enhance the analytical approach by constructing an analysis platform composed of another set of CFD/CSD analysis tools (UM-TURNS [15, 10] for CFD and DYMORE [16] for CSD). There are two main differences in the analysis framework used in this paper compared to that used by Bhagwat et al. [11]. The wake coupling methodology is utilized here in contrast to the wake capturing methodology. In addition the coupling of codes is performed using a python based framework where all data exchange is performed using memory pointers rather than file I/O making the coupling process efficient and seamless. The time evolution of the structural, fluid dynamic and vorticity transport equations are consistently coupled to obtain an aeroelastic solution for the unsteady maneuver.

## 2 Methodology

### 2.1 CFD solver

The Navier-Stokes equations are solved in their Reynolds-Averaged form which has been proven to be well-suited for high Reynolds number external flow problems as in the case of helicopter flight. After Reynolds-averaging, the Navier-Stokes equations govern the variation of the mean (time-averaged) flow quantities. Closure is achieved by accounting for turbulent fluctuations that are found using an adequate model that is dependent on the mean quantities (algebraic or equation based).

The RANS (Reynolds Averaged Navier-Stokes) solver used as the CFD analysis is the University of Maryland TURNS code [3, 8] which operates on meshes that follow structured-curved topology. The UMTURNS code uses a finite volume numerical algorithm that evaluates the inviscid fluxes using an upwind-biased flux difference scheme. The van Leer monotone upstream-centered scheme for conservation laws (MUSCL) approach is used to obtain third order accuracy, with Koren's differentiable flux limiters to make the scheme total variation diminishing. Viscous fluxes are computed using a 4th order central difference discretization. The Spalart-Allmaras one-equation model is used for the turbulence closure. The turbulence model equations are solved segregated from the mean-flow solutions and the necessary implicitness and time-accuracy is achieved using sub-iterations.

The LU-SGS scheme suggested by Jameson and Yoon [17, 18] is used for the implicit operator. Briefly, the LU-SGS method is a direct modification of the approximate lower-diagonal-upper (LDU) factorization to the unfactored implicit matrix. Though the (LU-SGS) implicit operator increases the stability and robustness of the scheme, the use of a spectral radius approximation renders the method only first order accurate in time. Therefore, a second order backwards difference in time is used, along with Newton-type sub-iterations to restore formal second order time accuracy.

UMTURNS uses the Arbitrary Lagrangian Eulerian (ALE) formulation for modeling unsteady flows with motion of the solid surfaces as in the case of helicopter flows. Calculation of the space and time metrics are the key requirements for the ALE formulation. The present numerical scheme employs a modified finite volume method for calculating the space and time metrics. Finite volume formulations have the advantage that both the space and time metrics can be formed accurately and free stream is captured accurately [19]. Also, it is to be noted that the computations include not only aeroelastic deformations but also gust fields that are generated by hub motion and wake transients. The space and time metrics are evaluated in such a manner that they implicitly satisfy the Geometric Conservation Law(GCL) and also maintain order of accuracy of the numerical scheme [9].

The computational domain is partitioned to facilitate calculations in a distributed computing environment. All parallel communications are achieved using the Message Passing Interface (MPI-2) standard.

#### 2.1.1 Calculation of Space and Time metrics

The strong conservation-law form of the Navier-Stokes equations in cartesian coordinates can be written as [20]

$$q_t + f_x + g_y + h_z = \sigma_x + \theta_y + \omega_z \quad (1)$$

$$q = (\rho, \rho u, \rho v, \rho w, \rho E)^T$$

$$E = e + \frac{u^2 + v^2 + w^2}{2}$$

$$f = (\rho u, p + \rho u^2, \rho uv, \rho uw, \rho uH)^T$$

$$g = (\rho v, \rho vu, p + \rho v^2, p + \rho vw, \rho vH)^T$$

$$h = (\rho w, \rho wu, \rho wv, p + \rho ww^2, \rho wH)^T \quad H = E + p/\rho$$

where  $u, v, w$  are the velocity components in the coordinate directions  $x, y, z$ ;  $\rho$  is the density,  $p$  is the pressure,  $e$  the specific internal energy; and  $\sigma, \theta, \omega$  represent the viscous stress and work

terms for each coordinate direction. Upon transforming to computational coordinates  $\xi, \eta, \zeta$  with the aid of the chain rule of partial derivatives, Eq.( 1) becomes:

$$\hat{q}_\tau + \hat{f}_\xi + \hat{g}_\eta + \hat{h}_\zeta = \hat{\sigma}_\xi + \hat{\theta}_\eta + \hat{\omega}_\zeta \quad (2)$$

$$\hat{q} = Jq$$

$$\begin{aligned} \hat{f} &= \hat{\xi}_t q + \hat{\xi}_x f + \hat{\xi}_y g + \hat{\xi}_z h & \hat{\sigma} &= \hat{\xi}_x \sigma + \hat{\xi}_y \theta + \hat{\xi}_z \omega \\ \hat{g} &= \hat{\eta}_t q + \hat{\eta}_x f + \hat{\eta}_y g + \hat{\eta}_z h & \hat{\theta} &= \hat{\eta}_x \sigma + \hat{\eta}_y \theta + \hat{\eta}_z \omega \\ \hat{h} &= \hat{\zeta}_t q + \hat{\zeta}_x f + \hat{\zeta}_y g + \hat{\zeta}_z h & \hat{\omega} &= \hat{\zeta}_x \sigma + \hat{\zeta}_y \theta + \hat{\zeta}_z \omega \end{aligned}$$

Here terms of form  $\hat{\xi}_{x,y,z}$ ,  $\hat{\eta}_{x,y,z}$  and  $\hat{\zeta}_{x,y,z}$  are the space metrics,  $\hat{\xi}_t$ ,  $\hat{\eta}_t$  and  $\hat{\zeta}_t$  are the time metrics in the computational domain, and  $J$  is the jacobian of the inverse coordinate transformation (i.e.  $J = \det\left(\frac{\partial(x,y,z)}{\partial(\xi,\eta,\zeta)}\right)$ ).

### 2.1.2 Field Velocity Approach

For the computations presented here, the vortex wake is computed using time accurate solutions of the vorticity transport equation. The effect of vortex wake is then coupled to the fluid equations using the field velocity approach [9] which is a way of modeling external velocity fields via apparent grid movement.

Mathematically, the field velocity approach can be explained by considering the velocity field,  $V$ , in the physical cartesian domain. It can be written as

$$V = (u - x_\tau)i + (v - y_\tau)j + (w - z_\tau)k \quad (3)$$

where  $u, v$  and  $w$  are components of the velocity along the coordinate directions and  $x_\tau, y_\tau$  and  $z_\tau$  are the corresponding grid time velocity component. Let the velocity induced by the external potential (e.g. that generated by the vortex wake) be represented by a velocity field  $(u', v', w')$ . Thus, the velocity field becomes

$$V = (u - x_\tau + u')i + (v - y_\tau + v')j + (w - z_\tau + w')k \quad (4)$$

The field velocity approach models this changed velocity field by changing the grid velocities. The modified grid velocities are defined as

$$\tilde{x}_\tau i + \tilde{y}_\tau j + \tilde{z}_\tau k = (x_\tau - u')i + (y_\tau - v')j + (z_\tau - w')k \quad (5)$$

Once the modified grid velocities are obtained, the grid time metrics in the computational domain  $(\hat{\xi}_t, \hat{\eta}_t, \hat{\zeta}_t)$  are computed as:

$$\begin{aligned} \hat{\xi}_t &= -(\hat{\xi}_x \tilde{x}_\tau + \hat{\xi}_y \tilde{y}_\tau + \hat{\xi}_z \tilde{z}_\tau) \\ \hat{\eta}_t &= -(\hat{\eta}_x \tilde{x}_\tau + \hat{\eta}_y \tilde{y}_\tau + \hat{\eta}_z \tilde{z}_\tau) \\ \hat{\zeta}_t &= -(\hat{\zeta}_x \tilde{x}_\tau + \hat{\zeta}_y \tilde{y}_\tau + \hat{\zeta}_z \tilde{z}_\tau) \end{aligned}$$

Detailed validation of this approach for model problems as well as full helicopter simulations can be found in Ref [9].

## 2.2 CSD solver

In the present study, the CSD code DYMORE is used for structural modeling. DYMORE is a finite element based tool for the analysis of nonlinear elastic multibody systems, developed at the School of Aerospace Engineering, Georgia Institute of Technology (Bauchau, Ref [16]). It includes a library of structural elements from which models with arbitrarily complex topologies can be built. The element library includes rigid bodies, cables, composite capable beams and shells, and joint models which can include generic spring and/or damper elements. Deformable bodies are modeled with the finite element method. The formulation of beams is geometrically exact, i.e. arbitrarily large displacements and finite rotations are accounted for, but is limited to small strains. The equations of equilibrium are written in a Cartesian inertial frame. Constraints are modeled using the Lagrange multiplier technique, resulting in a system of differential/algebraic equations (DAE). These equations are then solved using a robust an efficient time integration algorithm (Ref [21]).

### 2.3 Time accurate wake computations

The aerodynamic model incorporated in DYMORE utilizes 2-D airfoil theory augmented with airfoil table look-up. The inflow model is based on the theory for unsteady flow over a circular disk with a pressure jump across that disk [22]. In the present work, a free wake analysis is devised in an attempt to improve the inflow modeling and enhance the accuracy of rotor aerodynamics predictions.

The dominant structures in the rotor flow field are the blade tip vortices. The present analysis considers a single tip vortex filament on each lifting line of a rotor, released from each blade tip. The free wake problem is governed by the vorticity transport equation. Assuming that vortex elements convect with the fluid particles, the equation of evolution for the wake markers can be written as:

$$\frac{d\vec{r}(\psi, \zeta)}{dt} = \vec{V}(\vec{r}(\psi, \zeta)) \quad (6)$$

where  $\vec{r}$  defines the position vector of a wake marker, located on a vortex filament that is trailed from a rotor blade located at an azimuth  $\psi$ , and was first created when the blade was located at an azimuth  $(\psi - \zeta)$ , as represented in Figure 1.

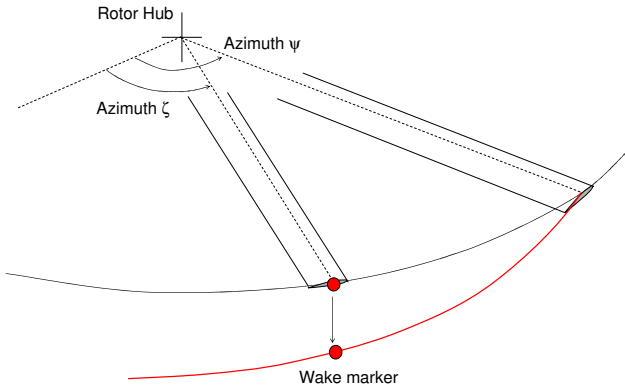


**Fig. 1** Representation of a wake free filament and a wake marker.

The vorticity transport equation can be written in the following partial differential form:

$$\frac{\partial \vec{r}(\psi, \zeta)}{\partial \psi} + \frac{\partial \vec{r}(\psi, \zeta)}{\partial \zeta} = \frac{\vec{V}(\vec{r}(\psi, \zeta))}{\Omega} \quad (7)$$

The right hand side velocity accounts for the instantaneous velocity field encountered by a marker on a vortex filament in the rotor wake. This includes the free-stream velocity, the induced velocities due to all the vortex filaments present in the wake, and also the induced contributions of the bound circulation representing the lifting rotor blades. This equation must be discretized into a set of finite difference equations that can then be numerically integrated. The time marching algorithm chosen is based on that suggested in Ref [23], and is modified to suit the present analysis framework [24].

The velocity term in the vorticity transport equation is computed from the Biot-Savart law:

$$\vec{V}(r) = \frac{\Gamma}{4\pi} \frac{h^2}{\sqrt{h^2 + r_c^2}} \int \frac{d\vec{l} \times d\vec{r}}{|\vec{r}|^3} \quad (8)$$

where  $\vec{V}(r)$  is the velocity induced at a point P located at  $r$  relative to the vortex element  $d\vec{l}$ . The integral is evaluated over the entire length of the vortex filament.  $\Gamma$  is the total strength of the filament, and  $d\vec{l}$  is an elemental unit vector along the vortex filament. The vortex core radius is noted  $r_c$ , and  $h$  is the perpendicular distance of the evaluation point from the influencing vortex element. Viscous diffusion is modeled by the growth of the core radius given by [25]:

$$r_c(\zeta) = \sqrt{r_{initial}^2 + 4\alpha\delta\nu\zeta/\Omega} \quad (9)$$

where  $\alpha$  is an empirical factor ( $\alpha = 1.25643$ ),  $\delta$  is the apparent viscosity coefficient, and  $\nu$  is the kinematic viscosity. The circulation  $\Gamma$  released at the blade tip is assumed to be equal to the maximum bound circulation along the blade. A near wake is included in the model to improve the accuracy of modeling the distortions created by the blades on trailed vortex wake. The blade bound circulation is fixed at the blade 1/4-chord and the near wake trailers emanate from these locations.

For operations within a table lookup based aerodynamic modeling flow boundary conditions are enforced at the blade control points that are located at the 3/4-chord location. This method provides a good first approximation to a lifting surface analysis, and is more accurate than a lifting line analysis [26].

For coupled operation with CFD, the blade bound circulations are computed based on the CFD aerodynamic loading and the enforcement of flow boundary conditions at 3/4 chord are turned off since they are implicitly satisfied by the higher resolution flow field solution from the CFD.

After the velocity contributions (Equation ( 8)) from both near and far wake are evaluated and aggregated at each wake marker location, the ordinary differential equations that denote the evolution of the wake markers are integrated in time using a 2nd order backward predictor-corrector algorithm (see Appendix in Ref [24]).

## 2.4 Fluid-structure interface

Since rotor blades have very little elasticity in the chordwise direction, they can be modeled quite accurately in the CSD methodology using a 1-D beam representation with flap, lag, axial and torsion degrees of freedom. In contrast, the entire surface of the blade is represented in the CFD mesh within the limit of grid resolution. The difference in geometry description of the CFD and CSD models requires specialized formulation for the transfer of loads and displacements. In this paper, we follow a rather simple approach of one-dimensional interpolation of sectional aerodynamic loading using cubic splines. Because of the structured nature of the grid, sectional aerodynamic loading can be easily determined using the pressure and shear stress distributions on the CFD surface grid. These are interpolated using cubic spline interpolation to the control points of the CSD model. As the span-wise resolution of the CFD mesh is commensurate (slightly higher) to that of the CSD control point distribution there is very little inconsistency between the total loading integrated in either solvers (i.e. this method

is force-preserving within the limit of grid resolution). Additionally, local continuity of loading is maintained because force/unit length is interpolated as opposed to the lumped-force itself.

## 2.5 CFD-Wake interface

The Eulerian fluid-dynamic equations ( 1) and Lagrangian wake equations ( 7) are interfaced using the field-velocity approach. At any time step, the wake coordinates obtained from the wake solver are used to evaluate the induced velocity field ( $u', v', w'$ ) at every grid point. The computation of the induced velocity field is expensive if a brute-force approach is followed. However, we utilize a fast-hierarchical approach [9] to accelerate this calculation which brings the associated computational overhead down to only about 10% of the total time step. Note that to prevent doubly accounting for the near-wake region (i.e region directly behind the blade), all the wake filaments that belong to a particular blade and are contained inside the CFD mesh belonging to that blade are not included in the induced velocity calculations. The CFD aerodynamic loading on the blade determines the bound vorticity and hence the amount of vorticity shed into the wake markers as described in Section 2.3.

In essence, the wake solver gives the wake positions, their circulation strengths and vortex diffusion parameters to the CFD solver. The CFD solver in turn provides the sectional aerodynamic loading to the wake solver such that the appropriate bound-vorticity profile can be computed.

## 2.6 Time integration procedure

The fluid, structure and wake equations are integrated using the conventional serial-staggered (CSS) time stepping scheme as shown in Figure 2. The CSS scheme was shown to provide similar levels of accuracy as fully time-accurate simulation (sub-iteration based) for a smaller computational overhead by Silbaugh et al. [14]. Therefore, this method is adopted for the present study. The sequence of integration is as follows: first the CSD solver computes converged blade position using the provided aerodynamic

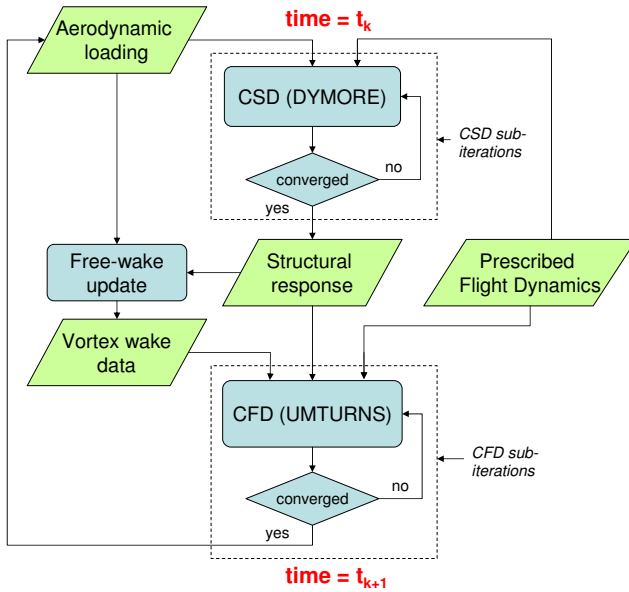


**Fig. 2** Schematic of the time-stepping sequence used for integration of governing fluid, wake and structural dynamic equations of the unsteady maneuver problem

loading, following that the wake solver computes new wake locations based on this new blade position as well as the provided aerodynamic loading. Once the new blade positions and wake locations are obtained, the fluid equations are integrated to generate the aerodynamic loading for the next time step. Note that this method not only degrades in accuracy but also shows instabilities if large time steps are used. In the present work, an azimuthal step of 0.4 deg is used. This value results in similar level of overall accuracy when using the serial-staggered scheme compared to the fully time-accurate simulation.

The initiation of the fluid-structure solution often creates large transients in both physical systems that can be amplified by the combined time integration procedure (because of its explicit nature) leading to destabilization. To prevent such destabilization from occurring, the CFD based aerodynamic loading is slowly introduced into the CSD loading using a smooth cosine decay scheme. The aerodynamic model (lifting-line based) is maintained active in the CSD solver for the initiation. This model is fully-coupled in the sub-iteration level and does not cause destabilization.

The aerodynamic loading from the CFD is slowly mixed with the lifting line aerodynamic loading over half a revolution of the maneuver. After the first half a revolution the lifting line modeling is completely turned off and the CSD loading is exactly equal to the CFD aerodynamic loading.

## 2.7 Python based coupling framework

The data transfer between the CFD and CSD/Freewake codes are facilitated in a python based framework. Python supports object-oriented programming and each participating solver is treated as an object (or module in Fortran90 parlance). The infrastructure executes legacy solvers but only after the solvers are “wrapped” with a socket-like Python layer. Python interfaces are compatible with other programming languages and there are freely available tools for developing these Python interfaces, such as *f2py* and *swig* for codes in Fortran90 and C/C++, respectively. Once wrapped, the participating solvers execute largely independent of one another following their own native parallel implementation. Different solvers can reference each other’s data through the Python layer using standard C-like pointers, without memory copies or file IO. However, the different solvers must accommodate common shared data structures maintained at the Python level for this to work efficiently. In essence, after the necessary wrapping procedures, the python script becomes the driver for the entire CFD/CSD simulation and orchestrates the appropriate time stepping and data exchange paradigms. In addition, it is also possible to run the Python wrapped code in parallel under MPI using *pyMPI* or *mympi*, allowing one to use the large scale parallel computers traditionally used for large-scale CFD calculations.

## 2.8 UH-60A aerodynamic and structural dynamic models

The mesh system used for the UH-60A rotor follows a C-O topology and is shown in Figure 3. The grid used for each rotor blade has 129 points in wrap around direction, 129 points in the spanwise direction and 65 points in the normal direc-

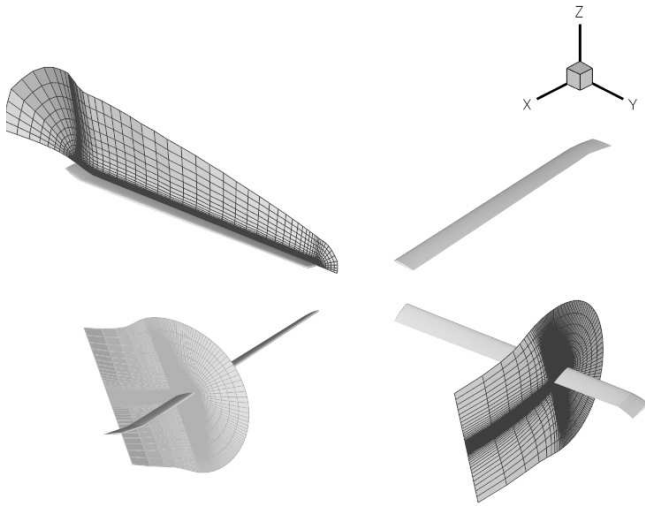


**Fig. 3 Mesh topology for UMTURNS wake coupling methodology**

tion respectively. The outer boundary of the grid extends about 3 chords from the blade surface. The full mesh system utilizes four such grids, one each for each rotor blade. Finer grid clustering is used in regions of high gradients such as the shed wake region (directly behind the trailing edge of the blade) and trailed wake region (at the root and tip of the blade). The wake coupling approach described in the previous section is used for including the returning wake effects.

Figure 4 shows a representation of the UH-60 rotor modeled using DYMORE. The rotor model consists of four elastic blades, each using 15 elements with cubic shape functions. The blade root articulation is modeled using three revolute joints, coincident at 4.66% blade radius. A rigid model of the rotor control system is used, including the pushrods, pitch horns, rotating and fixed swashplates. The pushrods are modeled as rigid elements connected to a prismatic joint with linear stiffness equal to 187792 lb/ft [11]. A model of the lead-lag damper is also included by modeling the damper as a rigid element connected to a prismatic joint with non-linearly varying damping coefficient.

The computations were conducted on a 16 processor cluster with Intel 2.3MHz chipsets. The wall clock time required/time step (including both CFD and CSD) for computations is noted to

be 2.2 seconds.

### 2.8.1 Validation of Aerodynamic Modeling

Figure 5 illustrates the improved prediction capabilities of the CFD based aerodynamic modeling compared to traditional lifting line based capabilities that are part of comprehensive analysis codes. Results are shown for the high speed flight condition of UH-60A helicopter. Identical set of blade motions that are obtained by forcing the structural model with measured flight test data is used for computation of aerodynamic loading in both lifting line and CFD approaches. The plots shown consist of aerodynamic loading (normal force and pitching moment) variation towards the tip of rotor and are representative of the overall quality of the results. It is evident that the CFD based aerodynamic modeling shows much improved agreement with experimental data for both normal force and pitching moment waveforms.

### 2.8.2 Validation of Structural Dynamic Model

The rotor blade frequency plot is shown in Figure 6(a) and (b), which correspond to two different values of pushrod stiffness, 62631 lb/ft and 187792 lb/ft, respectively. The larger stiffness value has been suggested as more accurate and is the one used in the present analysis [11]. However, the frequency variation results are presented for both stiffness values in order to allow comparison with published results using different comprehensive analysis (Ref [27, 28]). The predicted natural blade frequencies compare well with results from other analyses. The main effect of stiffening the pushrod is to increase the first torsional frequency from about 3.8/rev to about 4.2/rev. Other natural frequencies are not significantly affected.

## 3 UH-60A 11029 Maneuver description

The NASA-Army UH-60A Airloads Program investigated a wide range of flight conditions. Detailed measurements of blade aerodynamics and structural dynamics load measurements were

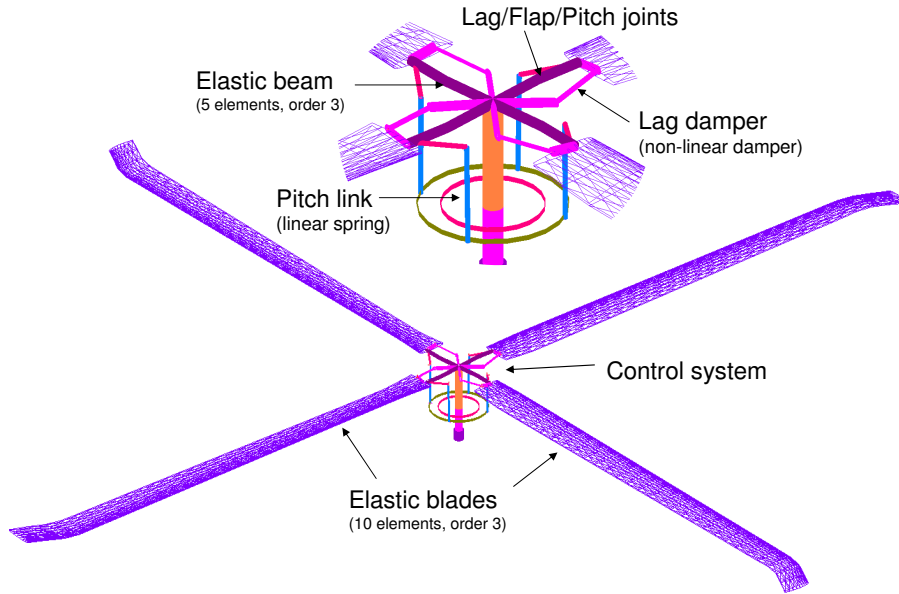


Fig. 4 Details UH-60A structural model used in DYMORE

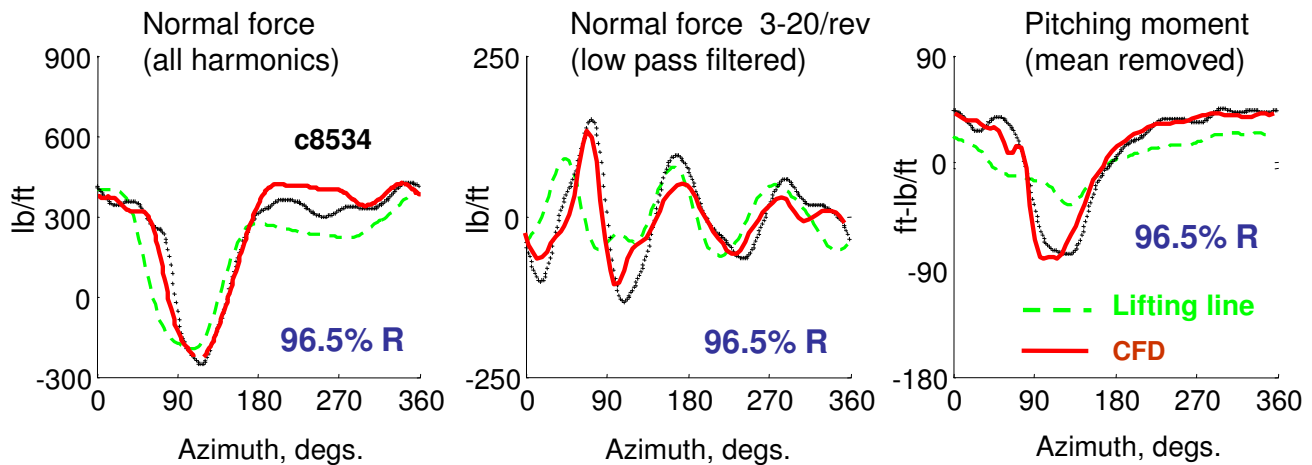


Fig. 5 Comparison of aerodynamic loading obtained from CFD and lifting line models for high speed forward flight condition

conducted which serve as a rich database for code validation. An extensive documentation of the flight test program can be found in Bousman and Kufeld [29, 30]. The operating envelope of the helicopters plotted as variation of vehicle weight coefficient with advance ratio is shown in Figure 7. The limiting factors for these flight conditions are the maximum thrust limit because of retreating blade stall and maximum sectional airfoil lift that can be generated. McHugh et al. [31] determined the maximum thrust bound-

ary using wind-tunnel tests which is represented in the figure. Note that all the steady flight conditions lie below the McHugh boundary. Figure 7 also shows the variation of weight coefficient with advance ratio for the UTTAS pull-up maneuver. The maneuver begins quite close to the maximum level flight speed of the aircraft and achieves a peak load factor of 2.1g, which exceeds the steady state McHugh boundary. Therefore the UTTAS pull-up maneuver is a challenging flight condition in terms of predictive capa-

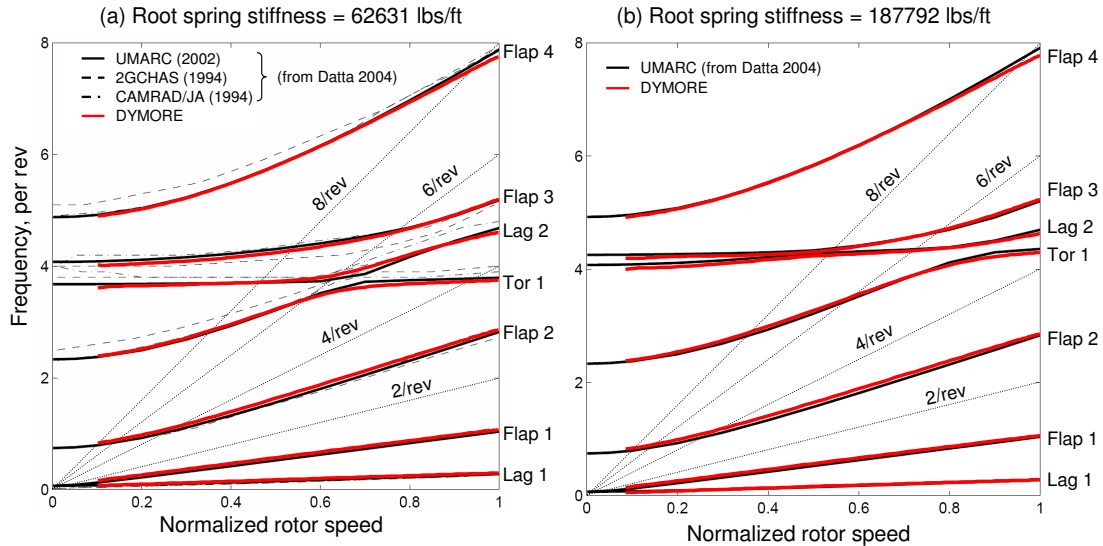


Fig. 6 Rotor frequency plot of UH-60A rotor obtained using the DYMORE structural dynamic model compared with those obtained from UMARC (Datta, 2005)

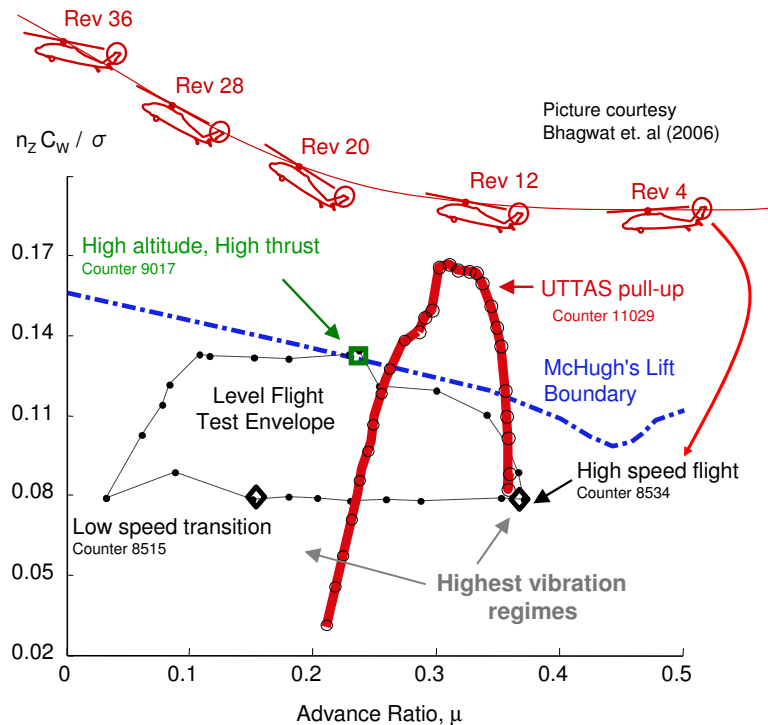


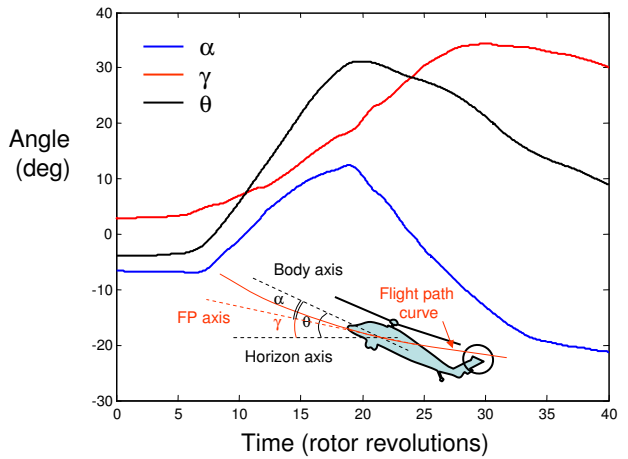
Fig. 7 UH-60A flight envelope and maneuver trajectory

bility. A schematic of the UH-60A pull-up maneuver is also shown in Figure 7 which consists of a transition from a level flight condition to a steady climb condition in about 40 revolutions of the rotor (approximately 10 seconds).

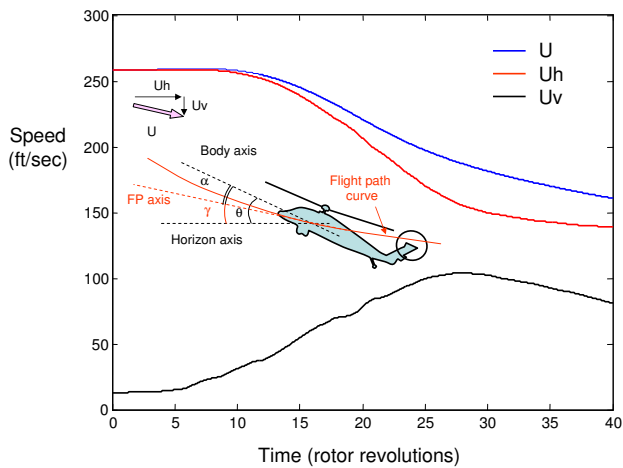
#### 4 Maneuver analysis

Simulation of free-flight maneuver requires the inclusion of a flight-dynamic model in the calculation of the aeroelastic response of the complete

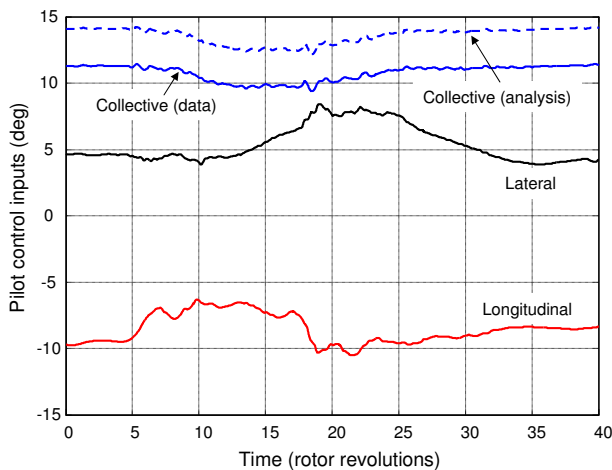
## Prediction of Helicopter Maneuver Loads using a Coupled CFD/CSD Analysis



(a) Vehicle attitude variation



(b) Flight path angle variation



(c) Pitch control variation

**Fig. 8 Prescribed flight dynamics and controls used for maneuver simulation**

rotorcraft. A few simplifications are introduced in the present study to reduce the complexity of the entire problem and facilitate validation. First, the pitch control inputs are prescribed rather than calculated in this analysis. Second, only the longitudinal dynamics of the maneuver is prescribed as it is the dominant contributor to the fundamental physical mechanisms.

The aircraft undergoes changes in attitudes as well as flight velocities owing to changes in flight path. In our approach, the attitude changes are modeled by actually rotating the grids to correspond to the vehicle orientation in space. In the Arbitrary Lagrangian Eulerian (ALE) CFD method, the rotational velocities and accelerations caused by attitude changes are computed using second order discretizations based on grid positions consistent with the geometric conservation law. Note that these rigid motions of the grid system are in addition to the aeroelastic deformations. The linear velocity changes are introduced using the field velocity approach, i.e. the grid velocities at all grid points are changed by the same magnitude and direction as prescribed by the flight dynamics at each time step. Note that these grid velocity changes are added to those introduced by the wake influence.

Figure 8 summarizes the variation of vehicle attitudes and pitch control variation. The angle of attack and pitch attitude response slightly lags the normal load factor response. The peak load-factor of 2.1g is achieved during revs 15-17 followed by peak pitch angle and angle of attack at rev 19-21. From revolution 19, the normal load factor diminishes gradually to 1 because of the gradual reduction of the aft cyclic input.

The collective control input is adjusted such that initial steady flight thrust levels are matched between analysis and experiment, i.e the trim procedure is performed only for matching the thrust and not the hub moments. Longitudinal and lateral cyclic controls are prescribed exactly as they were measured in the flight test.

Since the authors do not have full access to the actual experimental data base, the data shown in this paper are digitized from the publication by Bhagwat et al. [11, 13, 14]. All the experi-

mental data shown in this paper have been published elsewhere before by other research groups and could be considered public domain.

## 5 Results and discussion

### 5.1 Rotor performance

Figure 9 shows the comparison of the predicted rotor thrust compared with the total vehicle thrust computed using the normal load factor flight measurement. The normal load factor measurement includes contributions from fuselage/tail forces. The present analysis is restricted only to the rotor system and the thrust changes caused by the fuselage/tail aerodynamics are not modeled. Therefore, Figure 9 also includes the calculated rotor thrust obtained by integrating the measured sectional airloads.

The maneuver thrust is plotted as a function of time in units of rotor revolution. The oscillatory nature of the analysis results is because of the combination of unsteady aerodynamic load variations and hub accelerations. The measured data is statistically averaged over every revolution and hence appears smoother.

The general qualitative feature lift waveform (rapid increase at the beginning of the maneuver and gradual decrease to steady state at the end of the maneuver) are captured quite accurately by the analysis.

Some discrepancies in the quantitative comparison are expected since the effects of the fuselage and tail planes are not modeled in the current analysis, especially leading to underprediction of the maximum lift. Additionally the thrust variation during the recovery part of the maneuver is under-predicted by about 30% compared to the thrust integrated from the flight test aerodynamic loading. The reason for this discrepancy is not clear at the moment.

### 5.2 Wake Dynamics

The prediction of the unsteady wake dynamics is illustrated in Figure 10. Predicted vortex wake geometry follows expected qualitative trends corresponding to the prescribed flight dynamics and

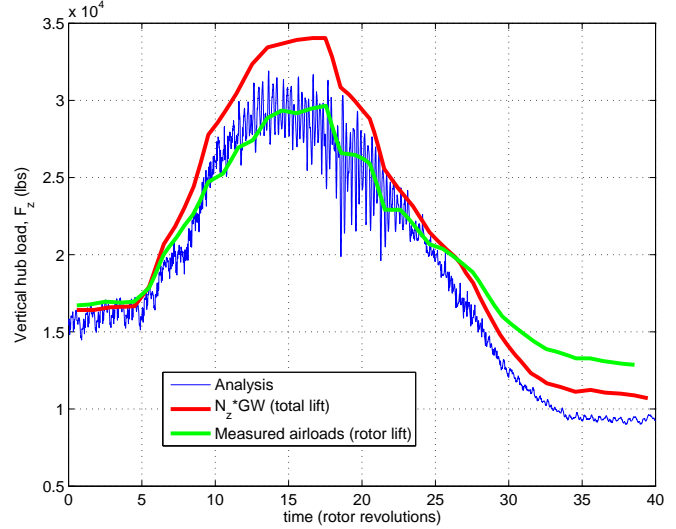


**Fig. 9 Predicted vs Measured total lift for the entire duration of the pull-up maneuver**

computed aeromechanics. At the initiation of the maneuver (rev 4), the operating condition is very close to steady high speed forward flight where the wake is convected away from the rotor system in the horizontal direction. Returning wake effects are minimal at this condition. The wake geometry shows asymmetrical roll-up in the rear view because of the large difference in the aerodynamic loading distributions on the advancing and retreating side of the rotor disk.

The aircraft angle of attack rapidly changes from nose-down to nose-up in the next 16 revolutions with the maximum angle of attack attained at the time level of about 20 revolutions. The vortex wake convects very close and even cuts through the rotor disk during this process. Therefore large unsteadiness can be noticed in the wake dynamics in the illustrations at rev 12 and rev 20. The combination of high thrust, higher climb rate and decreased forward speed at around revolution 20 causes increased vertical convection of the wake.

From revolution 20, the aircraft pitch attitude decreases gradually from its maximum value of 30 degrees. The aircraft angle of attack however decreases rapidly because of the increase in climb rate. The combination of aircraft pitch change and increased climb rate causes the vor-

# Prediction of Helicopter Maneuver Loads using a Coupled CFD/CSD Analysis

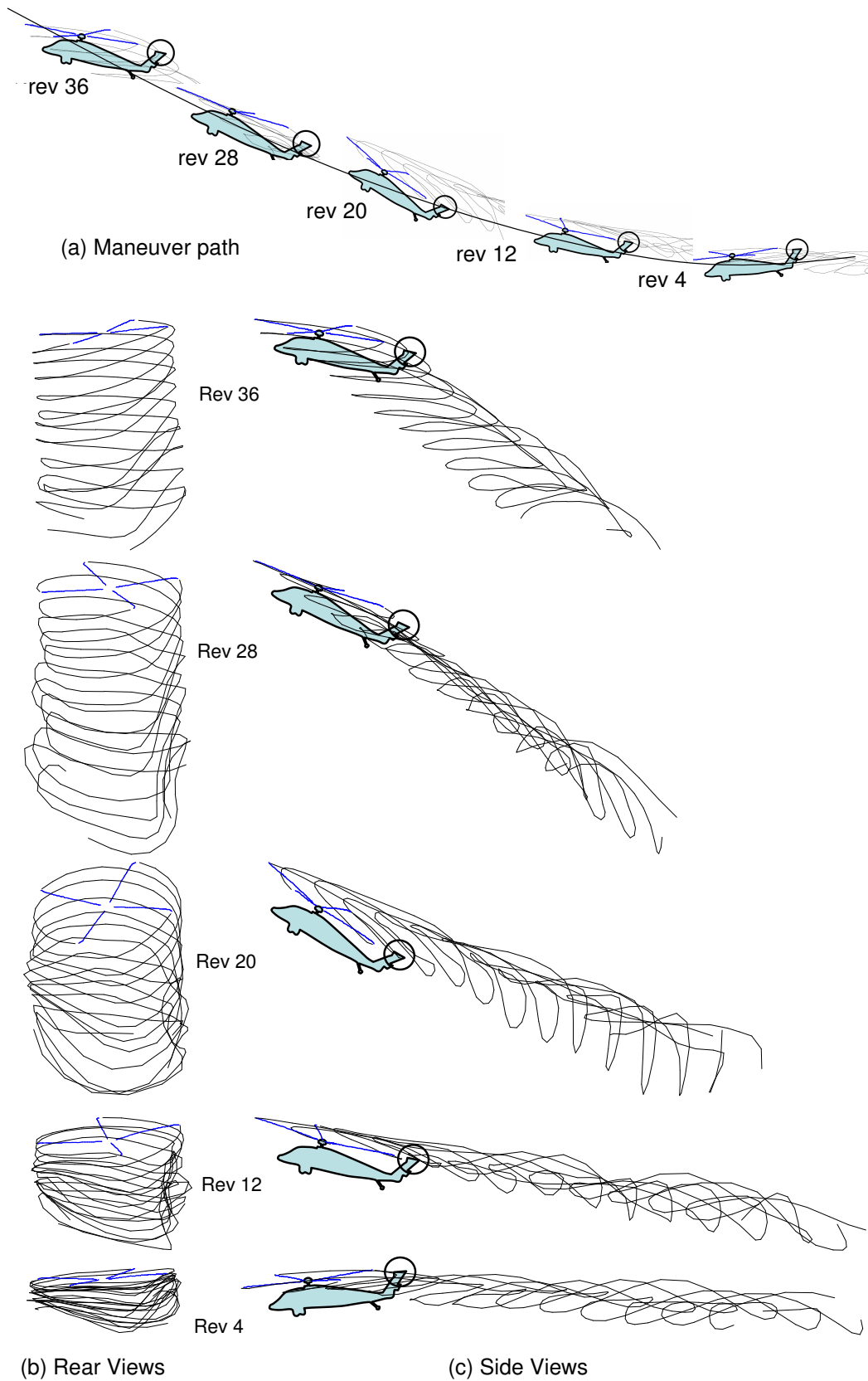


Fig. 10 Snap shots of unsteady wake dynamics during the course of the pull-up maneuver

tex wake to cut through the rotor-disk once again during the course of the maneuver producing associated aerodynamic loading perturbations. Towards the end of the maneuver at rev 36 the aircraft is climbing at about two-third its forward speed causing the wake to be spread vertically. The wake dynamics are benign at this condition because of the reduced thrust levels and a more even aerodynamic loading distribution on the rotor disk.

### 5.3 Aerodynamic loading prediction

The aerodynamic loading at various instances of the unsteady maneuver are illustrated in Figure 11 to Figure 14. Each figure shows the azimuthal variation of sectional normal force and sectional pitching moment (mean removed) at four chosen radial stations.

#### 5.3.1 Sectional normal force prediction

Overall the sectional normal force variation are well captured by the analysis for the entire maneuver. The normal force waveforms are dominated by the presence of advancing side negative lift gradient owing to transonics and retreating side negative lift gradient owing to flow separation. Fair prediction of the normal forces indicates that the analysis is able to predict the larger scale aeromechanics of this flight condition correctly. However, specific details of the waveform are not well captured, particularly the loading impulse on the advancing side, which may be caused by transonic stall. The normal forces are less sensitive to the actual aerodynamic loading along the airfoil compared to the pitching moments. Therefore the pitching moment variations constitute a more accurate metric to gauge the quality of the analytical results.

#### 5.3.2 Sectional pitching moment prediction

At the beginning of the maneuver (Figure 11), the operating condition is very close to high speed forward flight. The main characteristics of the waveforms of aerodynamic loading is the presence of negative lift and negative pitching moments on the advancing blade. From Figure 11 it

can be clearly seen that the CFD based aerodynamics predicts the pitching moment waveform quite accurately. This is because CFD provides accurate modeling of the advancing blade transonic effects (moving shock and shock relief towards the tip). Accurate prediction of sectional pitching moment leads to improved prediction of the elastic torsional response leading to improved prediction of effective angle of attack (which is a combination of control pitch, elastic torsion and inflow) at each blade section. Improved prediction of effective angle of attack in turn leads to improved prediction of advancing blade lift waveform.

As the aircraft engages on the longitudinal pull-up the pitch attitude and aircraft angle of attack increase leading to an increased thrust. The higher sectional angle of attack caused by the combination of control pitch, aircraft pitch rate and inflow transients causes flow separation and eventual stall on the retreating side of the rotor. The high frequency torsional response caused by the impulsive nose down pitching moment causes an elastic torsional response which relieves the high angle of attack momentarily causing the flow to reattach. However, within a few degrees of azimuthal sweep the elastic torsional response becomes out of phase with the control pitch inducing a higher sectional angle of attack and leading to another stall event. The presence of these two distinct stall events are most pronounced in revs 12-24 of the maneuver when the aircraft attains the maximum thrust level. The pitching moment excursions caused by the stall events are clearly visible in the sectional pitching moment plots (Figure 12(b), Figure 13(b) and Figure 14(b)). The analysis shows fair correlation in the prediction of these stall events. In particular, the magnitude of the stall events are underpredicted and the second stall cycle shows phase error with the experimental data. There is a third stall event clearly visible in the experimental data on the advancing side of the rotor disk. The analysis only predicts a weak stall event on the advancing side when compared with the experiment. This is consistent with the results obtained by Bhagwat et al. [12]. The inac-

curacies in the inflow distribution from the single tip free wake model may contribute to this under-prediction. Moreover, unsteady RANS computations suffer from large turbulence model sensitivities in resolving incidence of separation, reattachment and shock-boundary layer interaction, all of which are significant in this case.

As the aircraft recovers from the pull-up the higher angle of attack is relieved by a nose-down pitching attitude and pitch rate. This results in decreased intensity of the retreating blade stall events and disappearance of the advancing blade stall event (revolutions 23-24). The analysis shows improved correlation at these instances in resolving the pitching moment waveforms (Figure 14(b)).

### 5.4 Structural loading prediction

Accurate prediction of rotor blade structural loads is important for design considerations, and very challenging for this demanding maneuvering flight condition.

Four rotating frame loads are presented for comparison with test data: torsion moment at 30% R, pushrod force, normal bending moment at 50% R, and edgewise bending moment at 50% R. In each case, the variation of the half-peak-to-peak amplitude is presented, followed by the details of the waveform. For clarity and in order to allow comparison with published flight test data, the waveform plots are shown only for four selected 2-revolution frames spanning the maneuver: revolutions (1-2), (15-16), (19-20), and (23-24).

First, rotor blade torsion moment at 30% blade radius are represented in Figures 15 and 16. The torsion moment strongly correlates with the pushrod load, presented in Figures 17 and 18. Figure 15 shows that the peak-to-peak torsion moment trend is predicted satisfactorily, however the sudden increase in vibratory amplitude which occurs at around rev 7 in the test data is not predicted until rev 12, possibly due to the inaccuracies in stall prediction. The maximum torsion moment amplitude is also over-predicted by about 30%. However, details of the waveform

for key phases of the maneuver are well captured, as shown in Figure 16, which clearly shows the large stall-related oscillations on the retreating side under high normal loading, especially for rev 19-20.

The related pushrod load for blade 1 is shown in Figures 17 and 18, from which similar observations can be made: satisfactory prediction of the peak-to-peak amplitude, however with a 5-revolution delay in the onset of the amplitude increase, and good prediction of the key features of the waveform.

Results for the rotor blade normal bending moment at 50% blade radius are shown in Figures 19 and 20. For this blade load, both the peak-to-peak amplitude variation and details of the waveform are very well predicted, consistent with the accurate prediction of the sectional lift. However, the peak-to-peak amplitude of the normal bending moment is slightly under-predicted at the end of the maneuver (by a factor of 0.7). This is also consistent with the under-prediction of final total rotor thrust seen in Figure 9.

Finally, results for blade edgewise bending moments at 50% blade radius are shown in Figures 21 and 22. In this case, the peak-to-peak variation trend is captured satisfactorily, with maximum amplitude at around rev 20, but the amplitudes are the start and at the end of the maneuver are quite under-predicted (by a factor of about 0.4). Also, details of the waveform are not very well predicted for the edgewise bending moment compared to the other blade loads.

## 6 Conclusions

This paper presented correlation with test data for a tightly coupled CSD/CFD analysis simulating a maneuvering flight condition of the UH60A helicopter. The following conclusions could be drawn on the overall accuracy of the simulation:

1. The total rotor thrust variation during the maneuver is well predicted for the pull-up part of the maneuver, with a peak rotor lift close to 30000 lb. However, the rotor thrust variation during the recovery part of

the maneuver is under-predicted by about 30%.

2. Main features of the sectional lift variation are well predicted compared to flight test data for the entire duration of the maneuver. Advancing side transonics and retreating side flow separation that occurs at high load factors are well captured.
3. Sectional pitching moments are not predicted satisfactorily. The stall events occurring at high load factors on the retreating side of the rotor disk are captured but not resolved accurately; the advancing side transonic stall is not well captured.
4. Structural loads prediction is good for the normal bending moment at 50% R (both peak-to-peak variation and waveform), satisfactory for the torsion moment at 30% R and pushrod loads (increase in peak-to-peak amplitude delayed by about 5 revs compared to test data, good waveform prediction), and less than satisfactory for the edgewise bending moment at 50% R (large under-prediction of peak-to-peak amplitude).

This paper forms another link in the chain of research looking at improving the state-of-the-art in rotorcraft aeromechanics prediction. The results presented here agree with prior observations and further confirm the efficacy of CFD/CSD analysis in predicting aerodynamic and structural dynamic loading behavior during unsteady maneuvers. Moreover, the present study shows the capability of the wake coupling approach to produce results with similar levels of accuracy as the wake capturing approach. The wake coupling approach may be favored for preliminary design applications because of its faster execution time.

Significant modeling challenges still exist in further improving the prediction of rotorcraft aeromechanics. The most apparent ones that can be noted from the present work are in the prediction of stall incidence and reattachment which needs to be addressed by studies with higher

grid resolution as well as improved turbulence modeling. Moreover, current studies of rotorcraft maneuvers are still limited in scope because of they rely heavily on measured flight dynamic data. Therefore, another improvement that can be considered is full integration with flight dynamic modeling.

## 7 Acknowledgments

We acknowledge the support from the Army Research Laboratory with Dr. Mark Nixon and Matthew Wilbur as technical monitors. We thank Dr. Olivier Bauchau at Georgia Tech for providing the DYMORE code. We are grateful to Dr. Hyeonsoo Yeo, Dr. Mahendra Bhagwat, Dr. Robert Ormiston and Dr. Robert Kufeld at NASA Ames for sharing their thoughts and permitting usage of the published experimental data. We would also like to thank Dr. James Baeder and Ben Silbaugh from University of Maryland for reviewing the paper.

## References

- [1] William G. Bousman, "Putting the Aero Back Into Aeroelasticity", 8th Annual ARO Workshop on Aeroelasticity of Rotorcraft Systems, University Park, PA, October, 1999.
- [2] Datta, A., Sitaraman, J., Chopra, I, and Baeder, J., "Analysis Refinements for Prediction of Rotor Vibratory Loads in High-Speed Forward Flight", American Helicopter Society 60th Annual Forum, Baltimore, MD, June 2004.
- [3] Sitaraman, J., Datta, A., Baeder, I. and Chopra, I., "Coupled CFD/CSD Prediction of Rotor Aerodynamic and Structural Dynamic Loads For Three Critical Flight Conditions", 31st European Rotorcraft Forum, Firenze, Italy, Sep 13-15, 2005.
- [4] Potsdam, M., Yeo, Hyeonsoo, Johnson, Wayne, "Rotor Airloads Prediction Using Loose Aerodynamic/Structural Coupling", American Helicopter Society 60th Annual Forum, Baltimore, MD, June 7-10, 2004.
- [5] Altmikus, A. R. M., Wagner, S., Beaumier, P., and Servera, G., "A Comparison : Weak versus Strong Modular Coupling for Trimmed Aeroe-

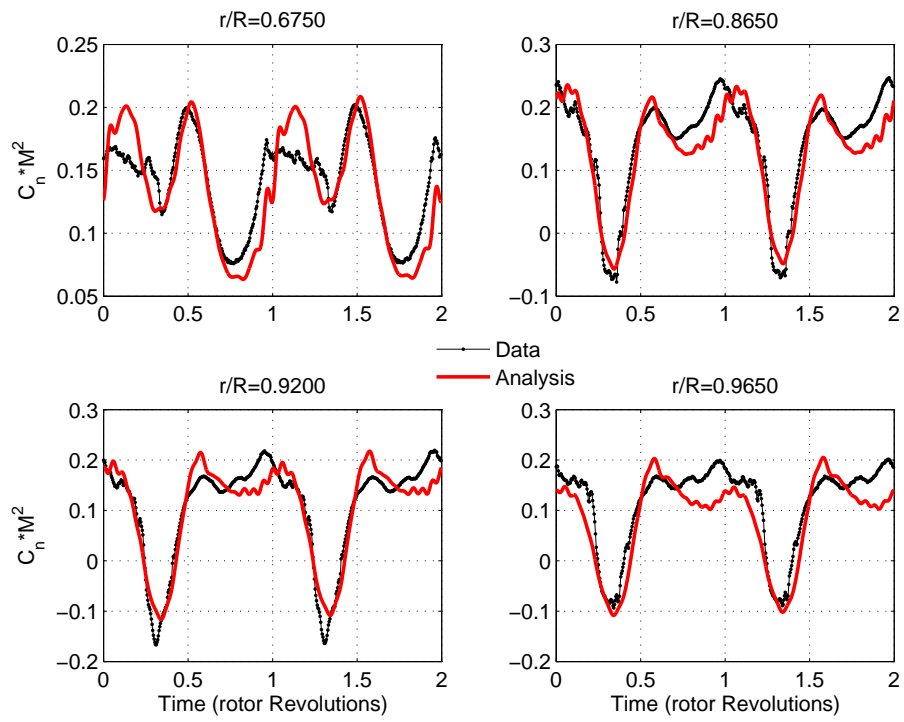
- lastic Rotor Simulation”, American Helicopter Society 58th Annual Forum, Montreal, Quebec, June 2002.
- [6] Pomin, H. and Wagner, S. “Aeroelastic Analysis of Helicopter Rotor Blades on Deformable Chimera Grids,” *Journal of Aircraft*, Vol. 41, No. 3, May-June 2004.
- [7] Sitaraman, J., Baeder J., D. and Chopra, I., “Validation of UH-60 Rotor Blade Aerodynamic Characteristics Using CFD”, 59th Annual Forum of the American Helicopter Society, Phoenix, 2003.
- [8] Duraisamy, K., Sitaraman, J. and Baeder, J., “High Resolution Wake Capturing Methodology for Improved Rotor Aerodynamic Computations”, 61st Annual Forum of the American Helicopter Society, Dallas, Texas, 2005.
- [9] Sitaraman, J., Baeder J. D., and Iyengar, V., “On the Field Velocity Approach and Geometric Conservation Law for Unsteady Flow Simulations”, 16th AIAA Computational Fluid Dynamics Conference, Orlando, Florida, June 23-26, 2003.
- [10] Sitaraman, J. and Baeder, J. D., “Evaluation of the Wake Prediction Methodologies used in CFD Based Rotor Airload Computations”, 24th Applied Aerodynamics Conference 5 - 8 June 2006, San Francisco, California.
- [11] Bhagwat, M., Ormiston, R., Saberi, H. and Xin, H., “Application of CFD/CSD Coupling for Analysis of Rotorcraft Airloads and Blade Loads in Maneuvering Flight”, 63rd forum of the American Helicopter Society, Virginia Beach, VA, May 1-3, 2007.
- [12] Bhagwat, M. and Ormiston, R., “Examination of Rotor Aerodynamics in Steady and Maneuvering Flight Using CFD and Conventional Methods”, AHS Specialists Conference on Aeromechanics, San Francisco, CA, Jan. 23-25, 2008.
- [13] Abhishek, A., Datta, A., and Chopra, I., “Comprehensive Analysis, Prediction, and Validation of UH60A Blade Loads in Unsteady Maneuvering Flight”, AHS Specialists Conference of the American Helicopter Society, Jan 23-25, San Francisco, 2008.
- [14] Silbaugh, B., and Baeder, J.D., “Coupled CFD/CSD Analysis of a Maneuvering Rotor Using Staggered and Time-Accurate Coupling Schemes”, AHS Specialists Conference on Aeromechanics, San Francisco, CA, Jan. 23-25, 2008.
- [15] Srinivasan, G.R., and Baeder, J.D., “TURNS: A Free-wake Euler/Navier-Stokes Numerical Method for Helicopter Rotors,” *AIAA Journal*, 31(5), 1993.
- [16] Bauchau, O. A. and Kang N.K., “A Multibody Formulation for Helicopter Structural Dynamic Analysis”, *Journal of the American Helicopter Society*, Vol 38, No 2, April 1993, pp 3 - 14.
- [17] Jameson, A., and Yoon, S., “Lower-Upper Implicit Schemes with Multiple Grids for the Euler Equations”, *AIAA Journal*, Vol. 25, No. 7, 1987, pp. 929-935.
- [18] Yoon, S. and Jameson, A., “An LU-SSOR Scheme for the Euler and Navier Stokes Equations”, AIAA paper 1987-600, Aerospace Sciences Meeting, 25th, Reno, NV, Jan 12-15, 1987.
- [19] Vinokur, M., “An Analysis of Finite-Difference and Finite-Volume Formulations for Conservation Laws”, *Journal of Computational Physics*, Vol.81, No.2, March 1989, pp. 1-52.
- [20] Pulliam, T. and Steger, J., “Implicit Finite Difference Simulations of Three Dimensional Compressible Flow”, *AIAA Journal*, Vol.18, No. 2, 1980, pp. 159-167.
- [21] Bauchau, O.A., Bottasso, C.L., and Trainelli, L., “Robust integration schemes for flexible multibody systems”, *Computer Methods in Applied Mechanics and Engineering*, 192(3-4):395-420, 2003.
- [22] Peters, D.A., and He, C.J., “Finite state induced flow models. Part II: Three-dimensional rotor disk”, *Journal of Aircraft*, Vol.32, 1995, pp. 323-333
- [23] Bhagwat, M. and Leishman, J. G., “Stability, Consistency and Convergence of Time-Marching Free-Vortex Rotor wake Algorithms”, *Journal of American Helicopter Society*, January 2001, pp 59-71.
- [24] Roget, B., “Simulation of Active Twist and Active Flap Control on a Model-Scale Helicopter Rotor”, 24th Applied Aerodynamics Conference 5 - 8 June 2006, San Francisco, California.
- [25] Squire, H. B., “The Growth of a Vortex in Tur-

- bulent Flow”, *Aeronautical Quarterly*, Vol. 16, August 1965, pp. 302-306.
- [26] Weissinger, J., “The Lift Distribution on Swept-Back Wings”, NACA TM 1120, March 1947.
- [27] Datta, A., “Fundamental Understanding, Prediction, and Validation of Rotor Vibratory Loads in Steady Level Flight”, Ph.D. thesis, University of Maryland at College Park, 2004.
- [28] Kufeld, R. M., Johnson, W., “The Effects of Control System Stiffness Models on the Dynamic Stall Behavior of a Helicopter”, American Helicopter Society 54th Annual Forum, Washington, D.C., May 20-22.
- [29] Bousman, G., and Kufeld, R. M., Balough, D., Cross, J. L., Studebaker, K. F., Jennison, C. D., “Flight Testing the UH-60A Airloads Aircraft”, 50th Annual Forum of the American Helicopter Society, Washington, D.C., May, 1994.
- [30] Kufeld, R. M., “High Load Conditions Measured on a UH-60A in Maneuvering Flight”, *Journal of the American Helicopter Society*, Vol. 43, (3), July 1998, pp. 202-211.
- [31] McHugh, F.J., “What are the lift and Propulsive Force Limits at High Speed for the Conventional Rotor ?”, American Helicopter Society 34th Annual Forum, Washinton D.C., May 1978.

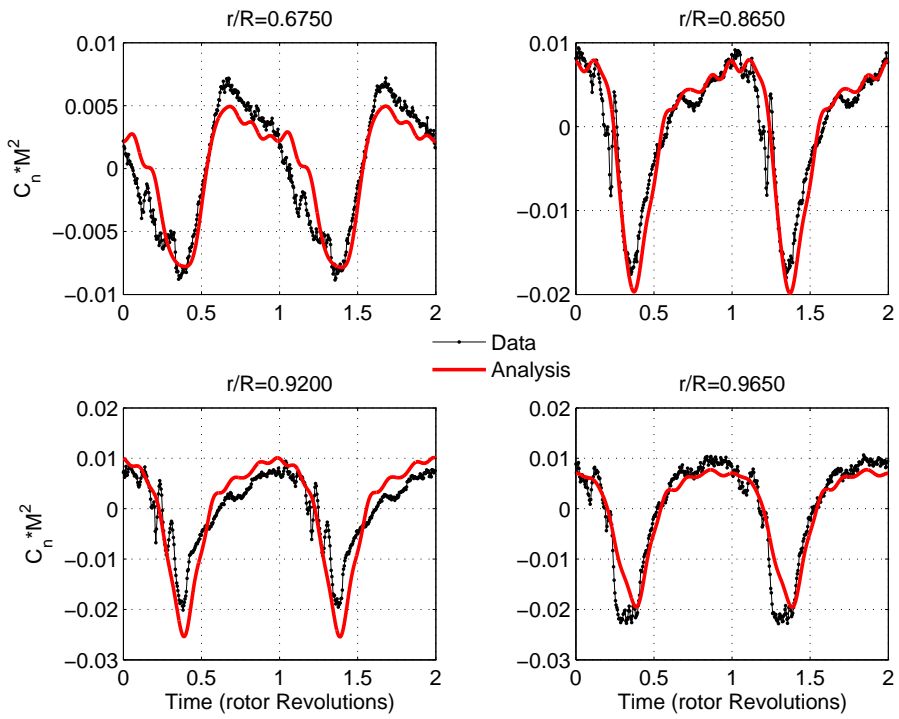
### Copyright Statement

The authors confirm that they, and/or their company or institution, hold copyright on all of the original material included in their paper. They also confirm they have obtained permission, from the copyright holder of any third party material included in their paper, to publish it as part of their paper. The authors grant full permission for the publication and distribution of their paper as part of the ICAS2008 proceedings or as individual off-prints from the proceedings.

## Prediction of Helicopter Maneuver Loads using a Coupled CFD/CSD Analysis

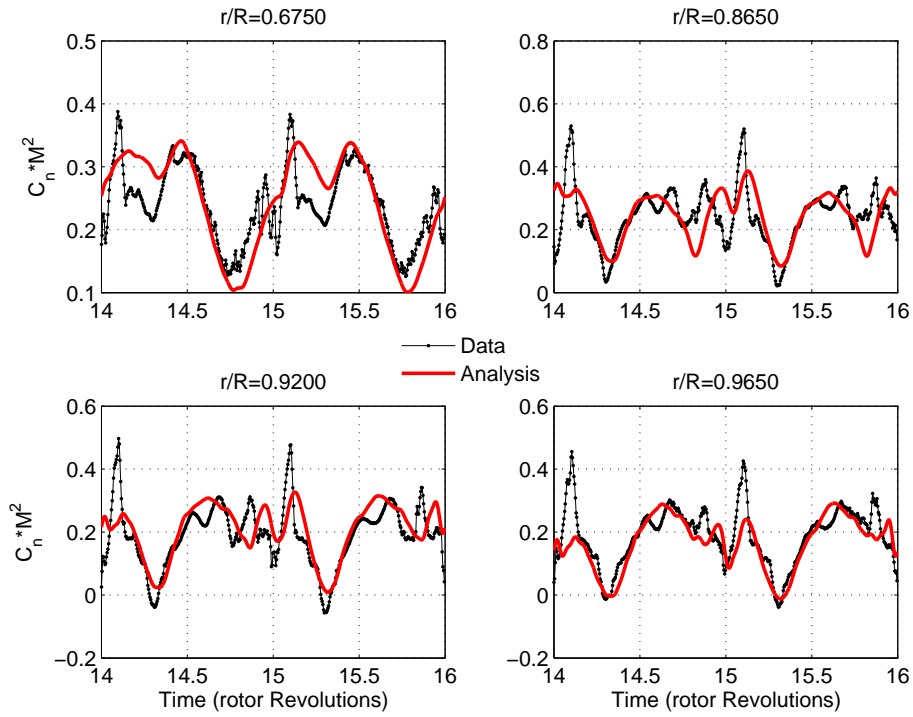


(a) Normal force variation

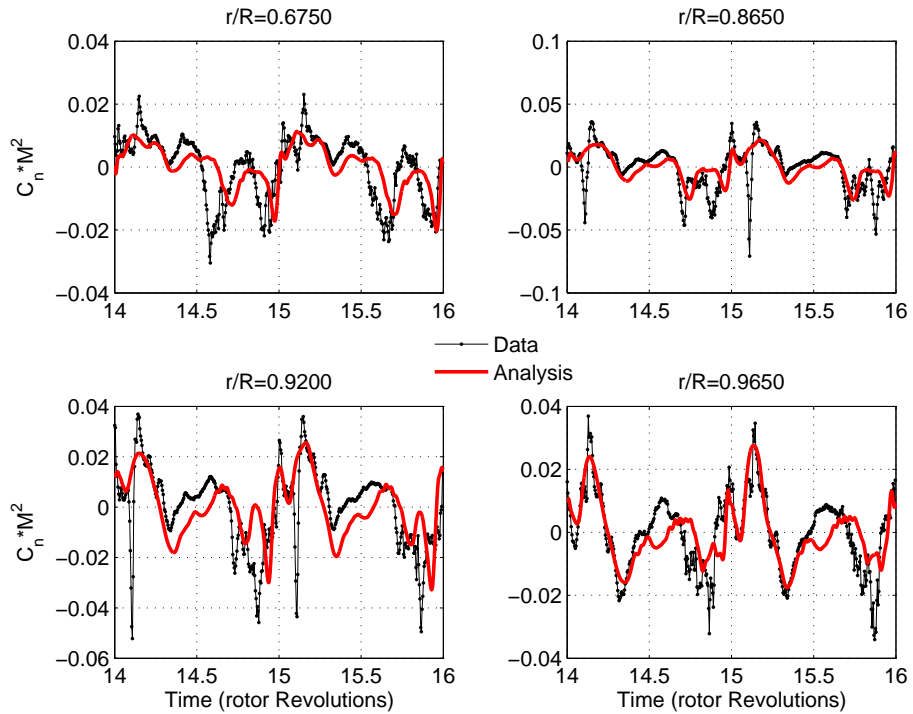


(b) Pitching moment variation (mean removed)

**Fig. 11 Non-dimensional sectional force variation with azimuth for the first two revolutions of the maneuver**



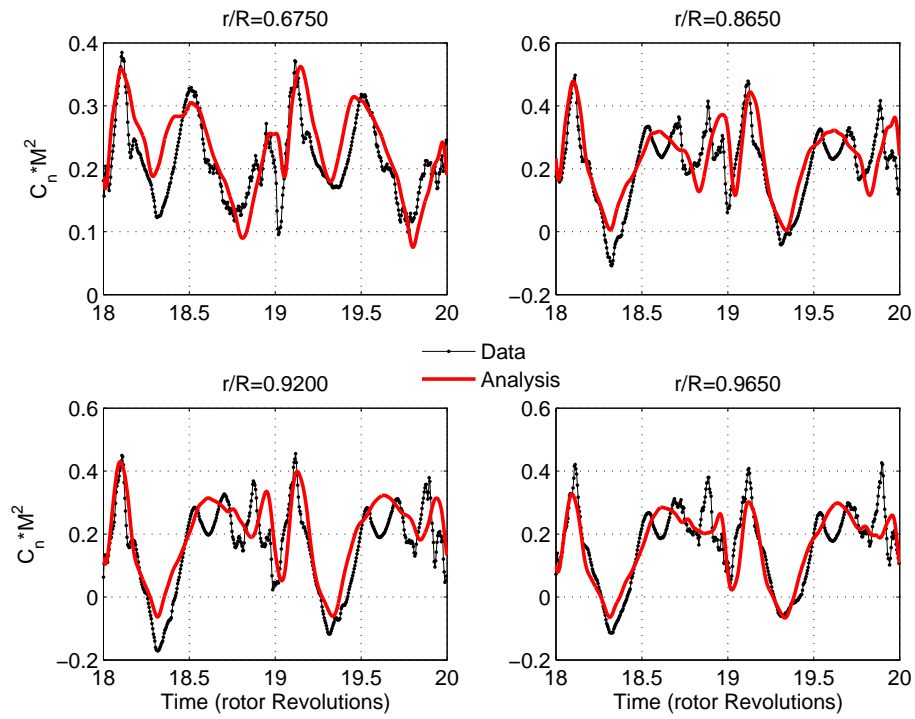
(a) Normal force variation



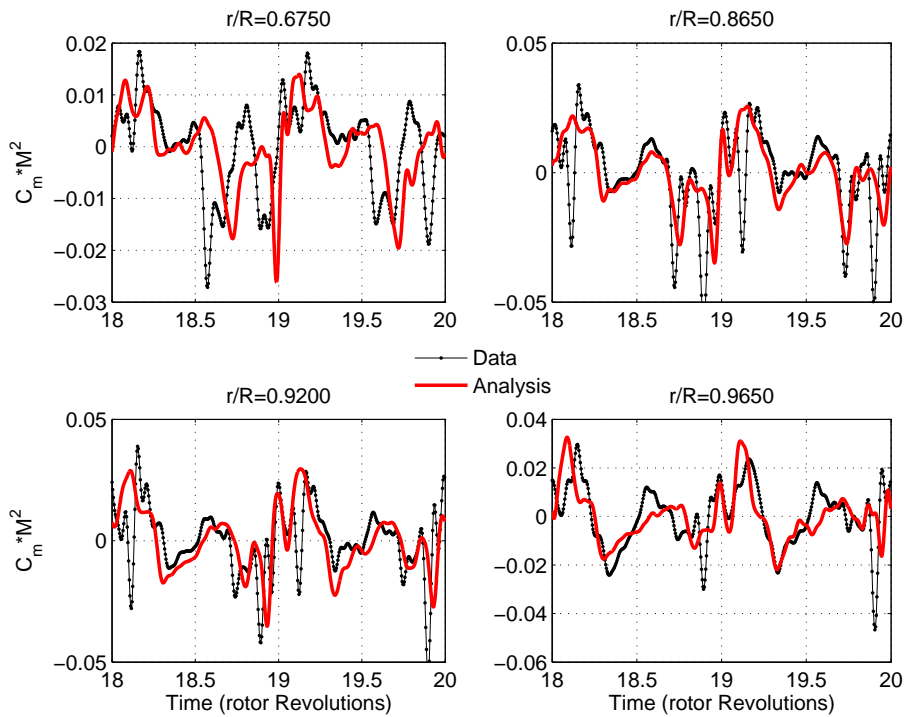
(b) Pitching moment variation (mean removed)

Fig. 12 Non-dimensional sectional force variation with azimuth for the revs 15-16 of the maneuver

## Prediction of Helicopter Maneuver Loads using a Coupled CFD/CSD Analysis

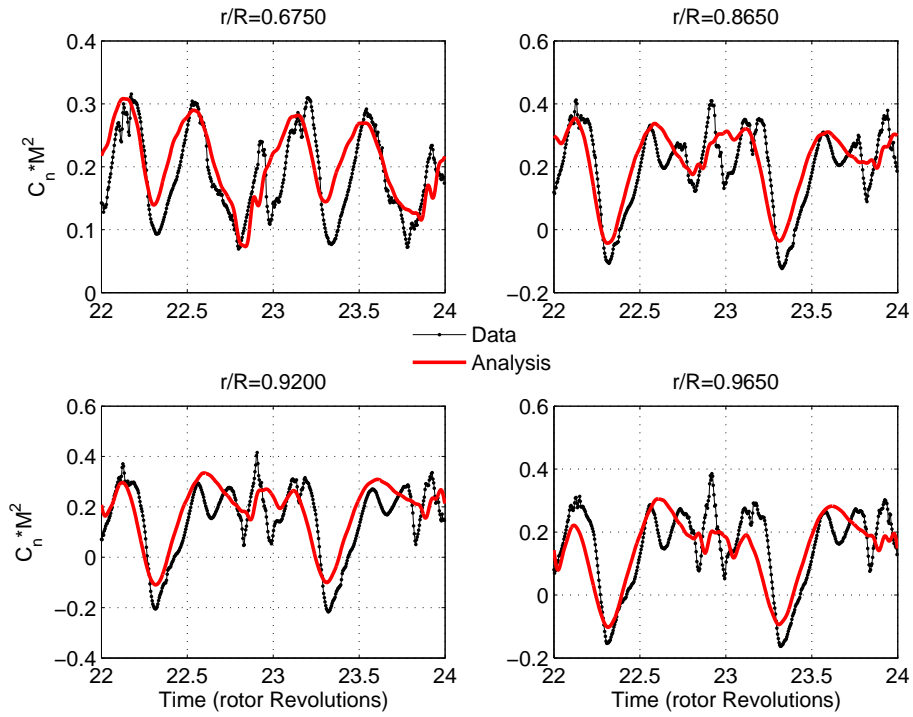


(a) Normal force variation

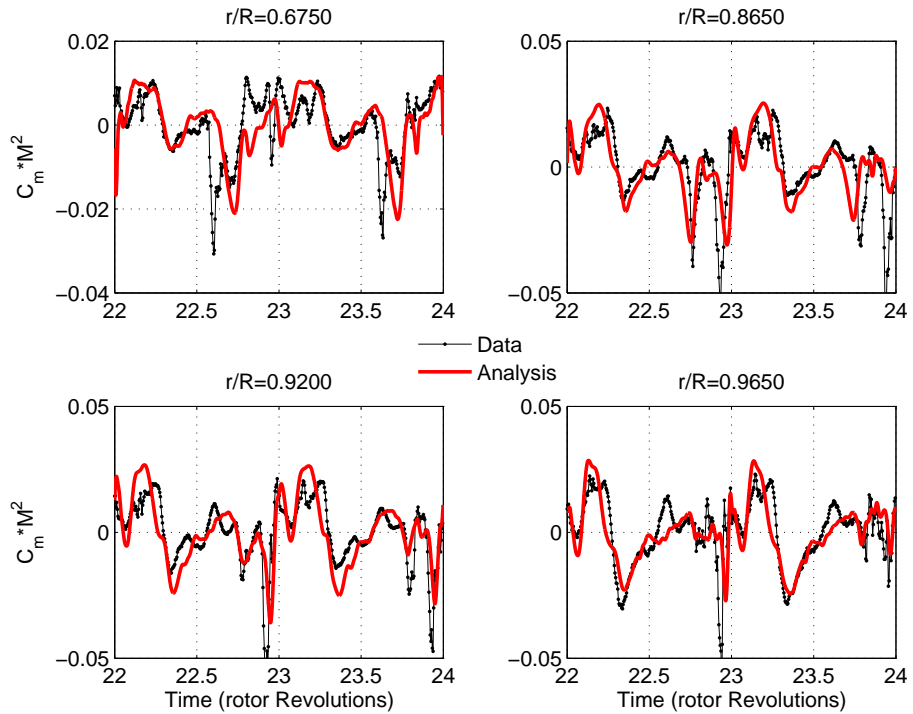


(b) Pitching moment variation (mean removed)

Fig. 13 Non-dimensional sectional force variation with azimuth for the revs 19-20 of the maneuver



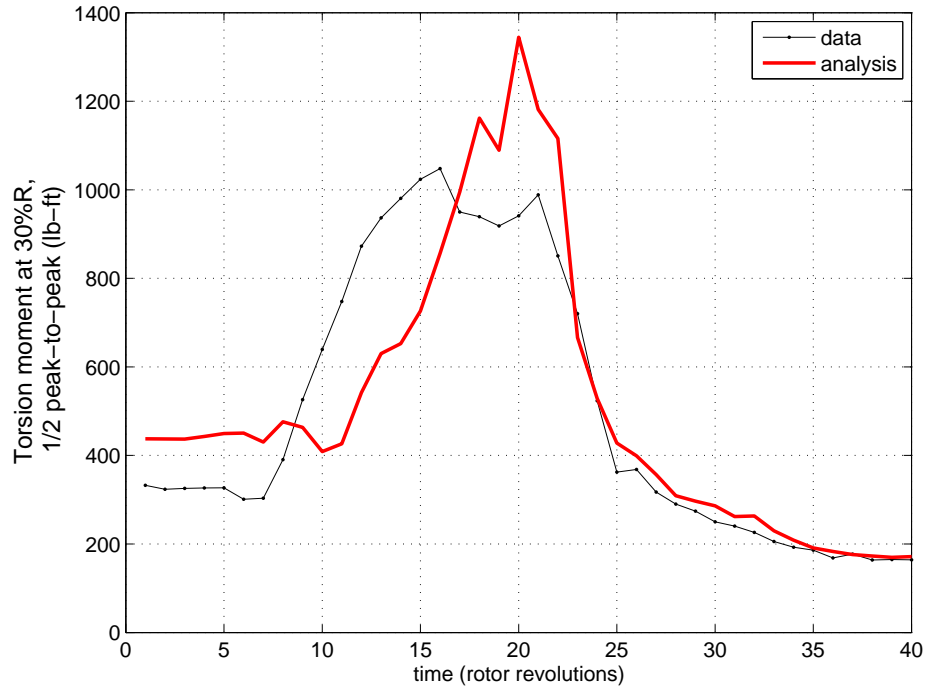
(a) Normal force variation



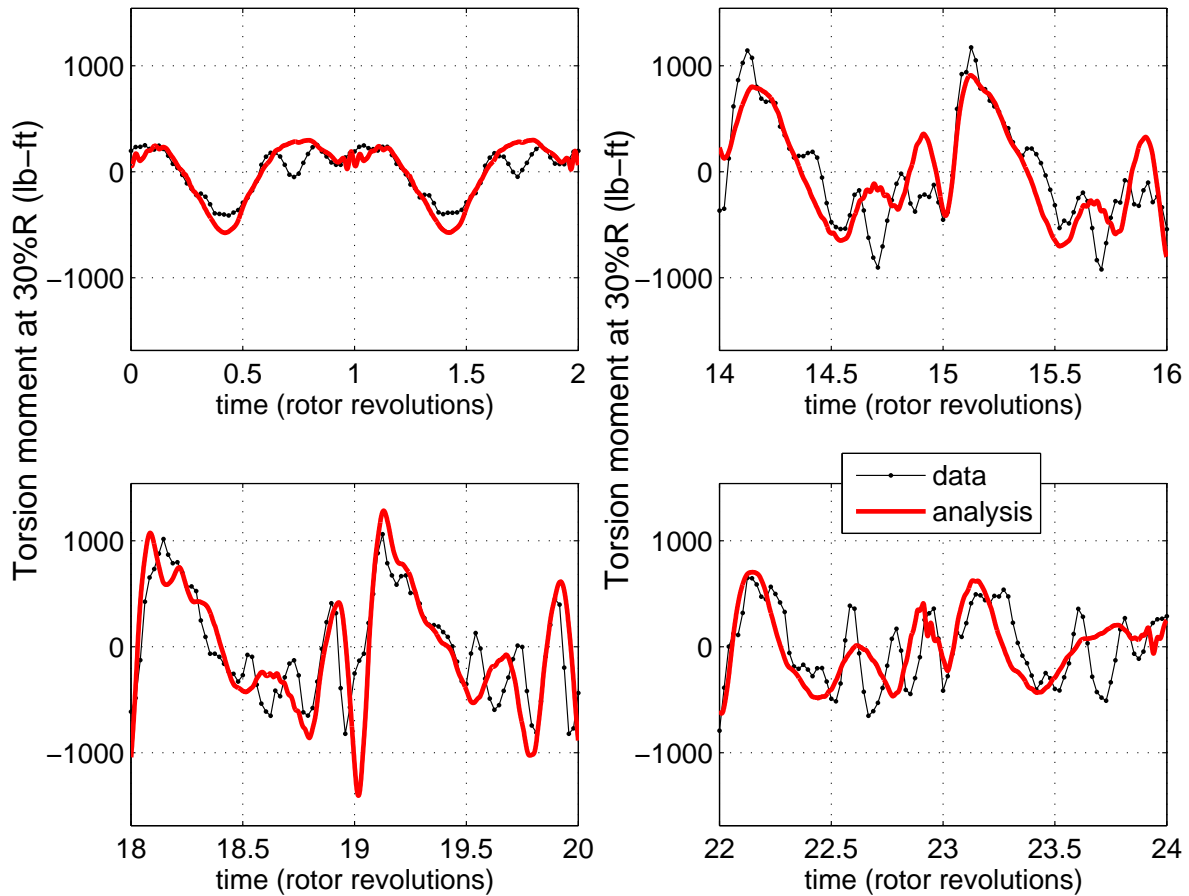
(b) Pitching moment variation (mean removed)

Fig. 14 Non-dimensional sectional force variation with azimuth for the revs 23-24 of the maneuver

## Prediction of Helicopter Maneuver Loads using a Coupled CFD/CSD Analysis



**Fig. 15 Torsion moments at 30%R, half peak-to-peak variation**



**Fig. 16 Torsion moments at 30%R, time histories (mean removed)**

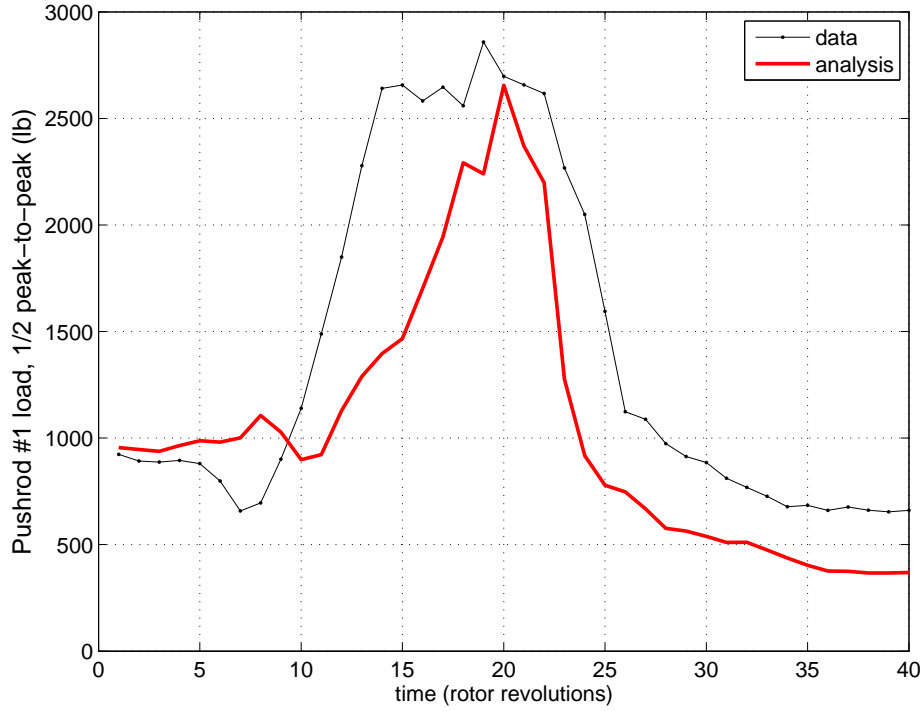


Fig. 17 Pushrod 1 load, half peak-to-peak variation

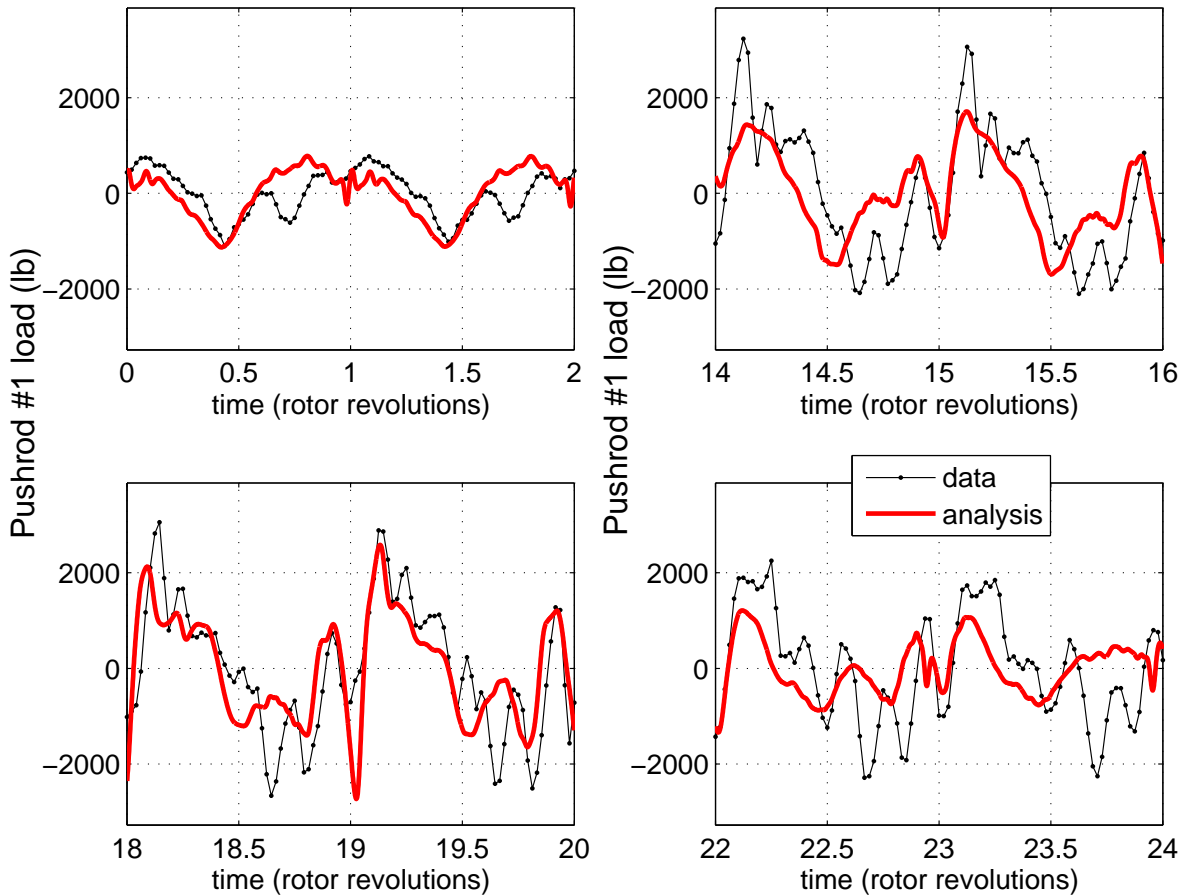


Fig. 18 Pushrod 1 load, time histories (mean removed)

## Prediction of Helicopter Maneuver Loads using a Coupled CFD/CSD Analysis

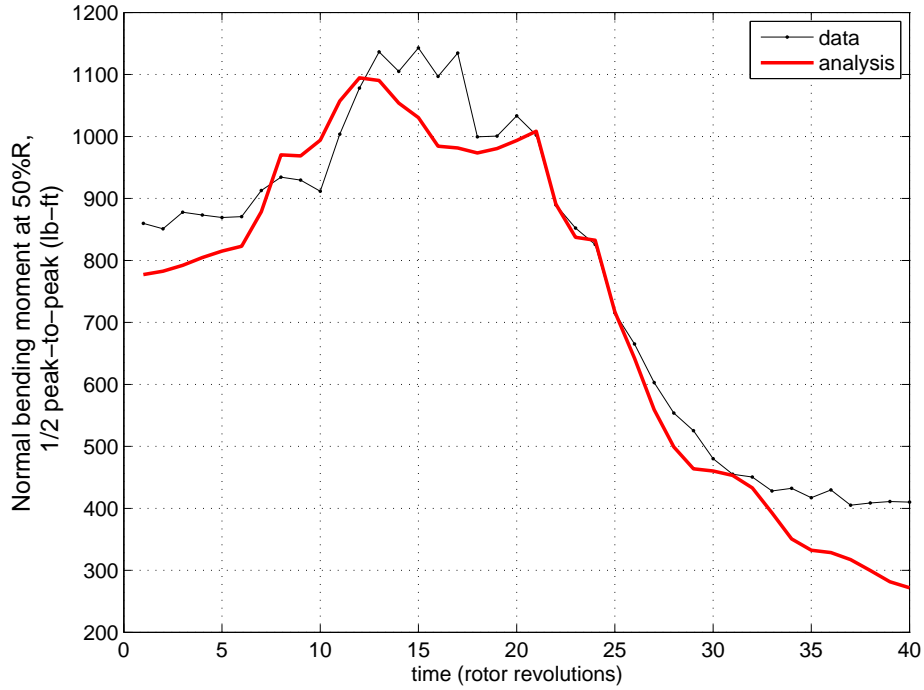


Fig. 19 Normal bending moment at 50% R, half peak-to-peak

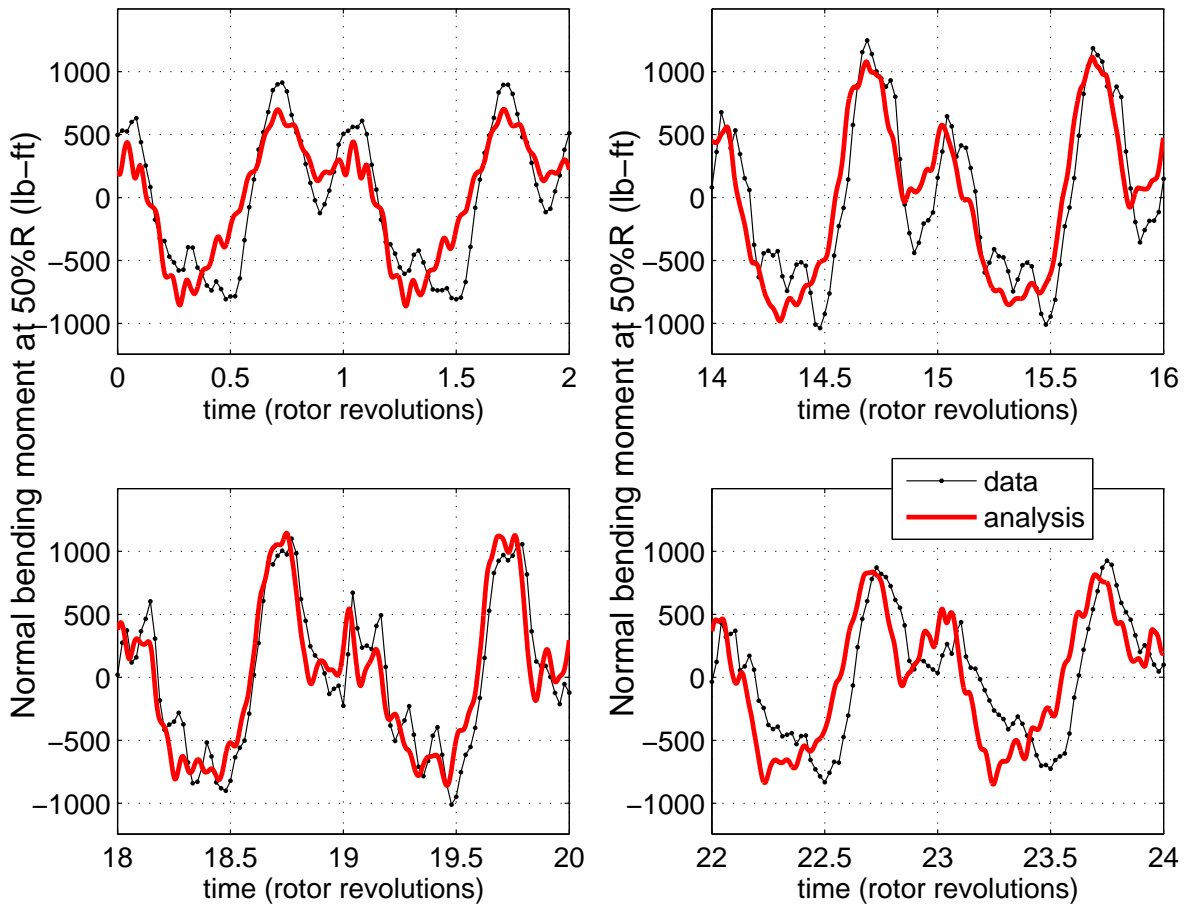
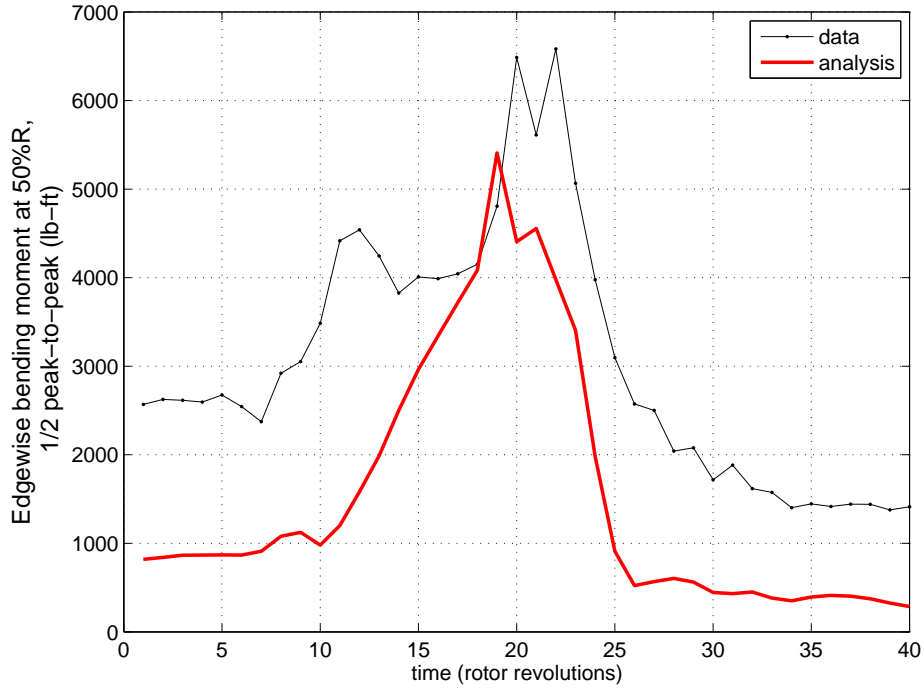
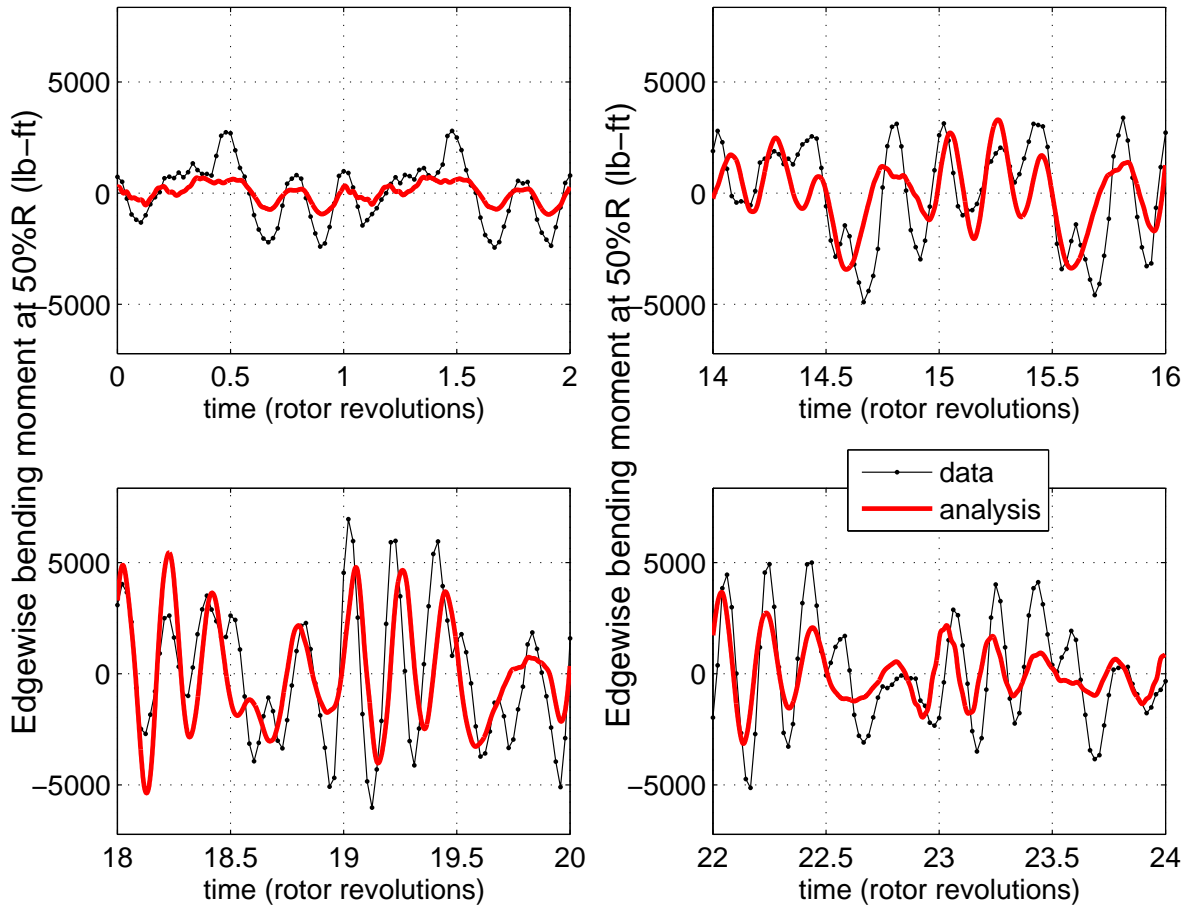


Fig. 20 Normal bending moment at 50% R, time histories (mean removed)



**Fig. 21 Edgewise bending moment at 50%R, half peak-to-peak**



**Fig. 22 Edgewise bending moment at 50%R, time histories (mean removed)**